Proceedings of the 16th European Turbomachinery Conference (ETC16)
Turbomachinery, Fluid Dynamics and Thermodynamics,
March 24-28, 2025; Hannover, Germany

Compressor tandem blade: investigation into actuation strategies

Mathias Brach[1], Andrea Rocca[2], and Koen Hillewaert*[1, 2]

[1]Department of Aerospace and Mechanics, Université de Liège, Allée de la découverte 9, 4000 Liège, Belgium
[2]Cenaero, Rue des Frères Wright 29, 6041 Charleroi, Belgium

Abstract

The outlet guide vane of the low pressure compressor is charged with redirecting the flow in the axial direction, thereby realising a very high turning, which results in relatively high losses and potential separation. The tandem blade concept allows to mitigate both aspects considerably by jettisoning the boundary layer midway of the passage from the first blade, and ensuring a very limited variation of the conditions upstream of the second blade, which realises most of the turning. Notwithstanding good performance of the tandem OGV, in particular considering the duty of the blade, there is still room for improvement, notably in the extension of the range towards high positive incidence incurred in the low mass flow rate regime. The paper provides a parametric study of the variable front blade tandem concept, which by varying the stagger angle of the front blade accommodates for a large incidence swing, while ensuring a constant outlet flow angle. The paper investigates the actuation strategy in function of incidence angle, indicating large gains in loss coefficient, pressure rise and operating range.

Keywords: low pressure compressor, outlet guide vane, tandem, variable stator vane, actuation

1 Introduction

Sustainability targets in aviation require radical innovation in engine design. In particular, engine manufacturers aim to improve performance while reducing weight. To achieve this goal, tandem blades are innovative geometries capable of providing greater flow turning with reduced overall losses compared to single-blade configurations, primarily due to a decreased number of vanes [1–5].

For this reason, they are good candidates to replace highly loaded stator vanes of axial compressor. However, despite good performance considering the duty of the tandem blade, there is still room for improvement, notably in the extension of the range towards high positive incidence incurred at low mass flow rate regimes.

This work focuses on the investigation of a hybrid configuration combining two strategies already available in the industry: tandem blades and variable vane settings. The first allows the boundary layer to develop along the blade to be separated into two boundary layers, the sum of which presents lower losses. The second concept is the variable stator setting. Currently this concept is used in *variable stator vanes (VSV)*, which pivot around an axis, thereby adapting the blade orientation with respect to the incoming flow and at the same time improving the incidence on the downstream rotor by changing the stator outlet flow angle. *Outlet Guide Vanes (OGV)* have a different role than SV, which precludes a general rotation of the blade since the outlet flow angle of the OGV is ideally fixed at 0°. The *variable front blade tandem (VFBT)* introduces a pivot on the first blade, which allows to reconcile the conflicting requirements of improving inlet incidence while maintaining a constant outlet angle. This is a unique additional advantage of using tandem blades for the OGV, and to the best of our knowledge, this is the first study on this concept.

In contrast to the VSV, the optimum rotational point is conditioned not solely by mechanical requirements, but predominantly by aerodynamic considerations since the relative position of the two blades is impacted. In this paper we present three intuitively chosen points, consisting of the trailing edge, a midchord position on the camber line and one inboard excentric point, whereas future research is focused on a comprehensive optimisation. Particular attention is directed towards high-incidence flows, as they are characterized by elevated pressure ratios, making them of significant interest in industrial applications.

The paper is organised as follows: first, it presents the tandem blades in its baseline geometrical configuration. The inlet Mach is equal to $Ma = 0.60$ and Reynolds number, based on the total axial chord, is equal to $Re_{c_{\text{ax}}} = 550k$. The flow angles here considered are $\alpha_1 = 36°$, $50°$ (nominal) and $60°$. α is measured w.r.t. the horizontal direction. The second part of the study will investigate combination of the tandem configurations with a variable front blade. The position of the center of rotation will determine the characteristics of the tandem.

The objective is to extend the incidence range of the blade in the classical sense, ie. keeping the total pressure loss below twice the minimal value.

2 Numerical Methods

The cascade performance is analysed using steady RANS simulations using the open-source suite $SU2$ (Economon et al. [6]). $SU2$ has several advantages particularly suitable for the present work, as it handles unstructured meshes, which allow easy meshing of the complex region between the two airfoils and can easily be exploited within an automatic workflow and in combination with other open-source software, in casu *Gmsh* [7] for pre-processing and *Paraview* [8–10] for analysis and

---

*Corresponding author: koen.hillewaert@uliege.be

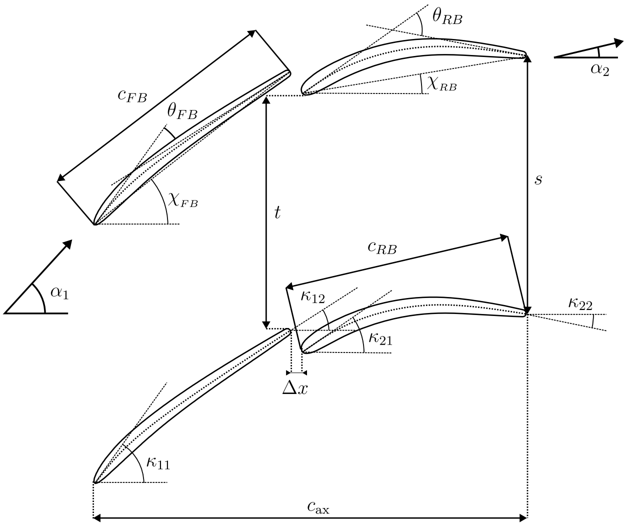

Figure 1: Tandem geometrical parameters

data visualization. Simulations were performed using the supercomputer *Lucia* of the Walloon region, operated by Cenaero.

3 Physical Modeling

The fluid is air here responding to ideal gas law, with specific heats γ and gas constant R. The dynamic viscosity μ is assumed to satisfy Sutherland's law [11]. The closure of steady compressible Reynolds-Averaged Navier-Stokes (RANS) is obtained employing Boussinesq hypothesis [12]. The turbulent viscosity μ_T is obtained from Shear-Stress Transport (SST) turbulence models (Menter et al. [13]).

4 Application Case and Numerical Setup

4.1 Brief Description of Tandem Blades

Figure 1 shows the geometry of the two blades and the geometrical parameters. Readers interested in a more exhaustive introduction to tandem blades can refer to [14]. We indicate the flow angle with α, the tangent to the blade skeleton with κ, and the angle between the chordline and the horizontal with χ. The *incidence angle* is the angle between the flow and the first blade $i = \alpha_1 - \kappa_{11}$. The *axial overlap* is a measure of the gap between the two blades. It is defined as $\mathrm{AO} = \Delta x / c_{\mathrm{ax}}$ where c_{ax} is the total axial chord, measured from the leading edge of the front blade to the trailing edge of the rear blade. The reduced pitch t is defined as the distance between the trailing edge of the first blade and the leading edge of the second blade in the next tandem blade. Finally, the percent pitch PP is defined as the ratio between t and the pitch s.

4.2 Numerical Setup

The blades are considered in cascade configuration and the flow is bi-dimensional with the axial velocity-density ratio equal to one. Since periodic boundaries are imposed in the pitch-wise direction, it follows that only inlet and outlet boundary conditions have to be set.

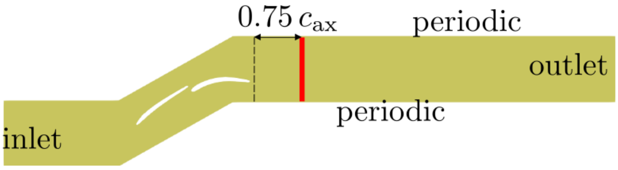

Figure 2: Computational domain

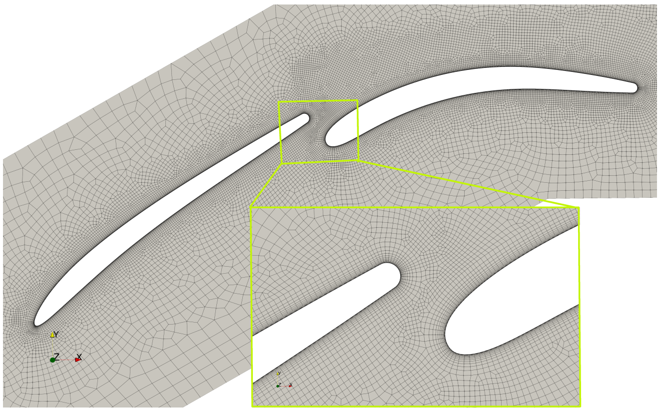

Figure 3: Visualization of computational grid

Figure 2 shows a schematic representation of the computational domain, where the name of the boundaries are also indicated. In particular, at inlet we impose total pressure $p_{0,1}$, total temperature $T_{0,1}$ and flow angle α_1; the static pressure p_2 is imposed at the outlet. The latter needs to be iteratively adjusted to fix the inlet Mach number Ma_1 and consequently Reynolds number Re_1.

The inlet turbulence intensity is equal to $TI = 5\%$ and turbulent-to-laminar viscosity ratio to $\mu_T/\mu = 10$. Note that some of the results presented below are based on two measurement planes, one located at inlet, indicated by subscript "1", and one close to the outlet, indicated by subscript "2". The outlet plane is placed at 0.75 c_{ax} from the trailing edge of the rear blade (see Figure 2).

The mesh is shown in Figure 3 and is selected following a mesh-refinement study, where the Mach number is measured $0.75c_{\mathrm{ax}}$ downstream the trailing edge of the rear blade. The Root-Mean-Squared error between two different meshes is computed and shown in Table 1. Mesh number 3 is utilized.

Mesh number	**Number of cells**	**RMS error ε_{RMS} [%]**
0	4250	-
1	8419	5.52
2	17 469	3.93
3	35 053	1.21
4	69 878	0.72

Table 1: Mesh refinement study

Figure 4 shows that mesh requirements for wall resolved computations are fulfilled. The first cell center is placed at

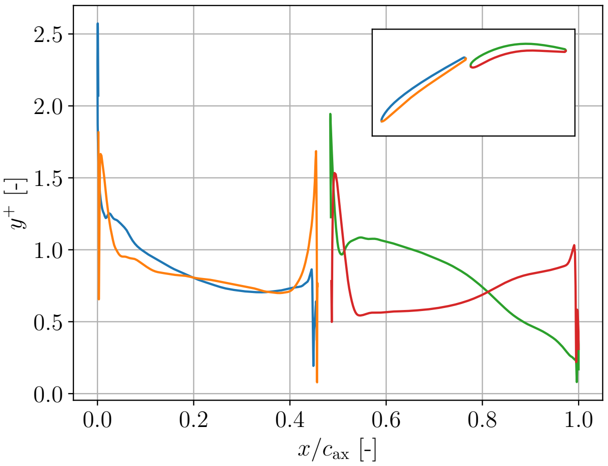

Figure 4: Blade wall-resolution in viscous units

approximately one viscous unit from the wall, $y^+ \approx 1$, with $y^+ = \rho y_1 u_\tau / \mu$, where u_τ is the friction velocity and y_1 is the distance from the wall of the cell center of the local wall-adjacent cell. The mesh quality is rather high, as the maximum mesh Skewness is $S = 0.75$, while the Aspect Ratio is $AR = 100 - 400$.

The gradients of the flow variables are computed using the weighted least-square approach, while the advective term is discretised by an unstructured Jameson-Schmidt-Turkel scheme, which features fourth order scalar dissipation with coefficient $\alpha_4 = 0.02$, switching to a second order dissipation with coefficient $\alpha_2 = 0.5$ in the presence of shocks. The advective terms of the turbulence variables are discretized with a first order upwind scheme. The algebraic linear system of equations is solved iteratively with the Flexible Generalized Minimum Residual (FGMRES) approach.

5 Results

This section presents the results of the simulations carried out for different front airfoil stagger angles χ_{rel} or equivalently inlet metal angle κ_{11} (see Figure 1). In subsection 5.1, the initial configuration is presented, *i.e.* the tandem configuration with no changes in the front airfoil angle. This configuration is used as benchmark for comparison with the other cases. Successively, the front airfoil angle χ_{rel} is defined as the angle of rotation with respect to the front blade initial position.

5.1 Baseline Configuration

In this section the flow field is presented; for the sake of conciseness, this visualisation will not be repeated for the other cases. Figure 5 shows the contour plot of the Mach number. We can clearly notice, that the wake of the front airfoil contributes to bound the flow which passes through the gap, and accelerates along the suction side of the rear airfoil. The gap between the airfoils resets the boundary layer, resulting in a higher resistance to the adverse pressure gradients which allows the tandem to realise an important turning on the flow.

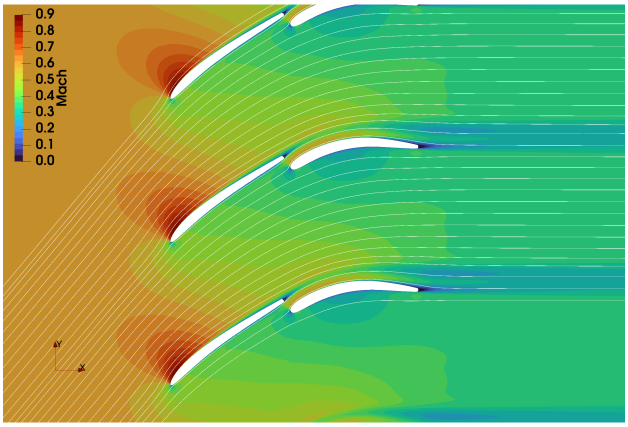

Figure 5: Flow Mach number for $\alpha_1 = 50°$ and $\chi_{rel} = 0$.

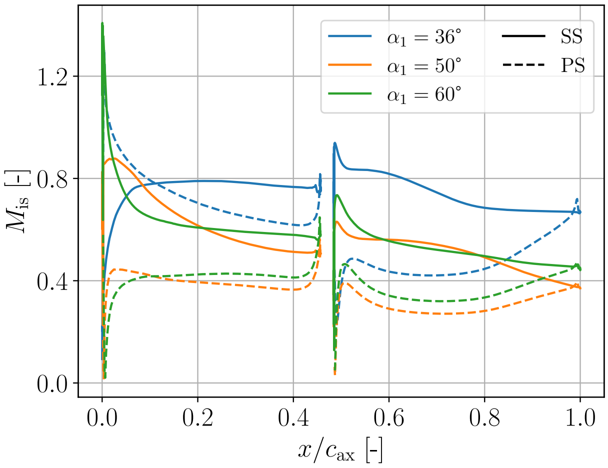

Figure 6: M_{is} for $\chi_{rel} = 0$ and various α_1-angles.

We now compare the optimum flow configuration ($\alpha_1 = 45°$, orange curves) to limit values in negative incidence ($\alpha_1 = 36°$, blue curves) and positive incidence ($\alpha_1 = 60°$, green curves) which are not too far outside of the operating range of the airfoil. Figure 6 shows the airfoil loading by means of the isentropic Mach number, defined as

$$M_{is} = \sqrt{\frac{2}{\gamma - 1}\left(\left(\frac{p_{0,1}}{p}\right)^{\frac{\gamma-1}{\gamma}} - 1\right)}. \qquad (1)$$

for three different incidence angles. At optimum incidence angle (flow angle $\alpha_1 = 45°$, orange curve) the flow is almost parallel to the camber line at the leading edge. The airfoil camber deviates the flow in absence of flow separations and detachments. On the pressure side of the front airfoil the load remains almost constant. Differently, on the Suction Side (SS), the load increases considerably along the airfoil (M_{is} decreases). For positive incidence angles, as for instance $\alpha_1 = 60°$, indicated by green color, we observe much sharper pressure gradients, especially on SS, but the same qualitative behavior as seen for $\alpha_1 = 45°$. At negative incidence angle, as shown by the blue curves, the airfoil SS is under pressure and vice-versa. The flow accelerates around leading edge towards the Pressure Side (PS) and therefore the Mach distribution swaps. The airfoil loading on the PS increases in the first part of the airfoil and then stays constant. At this incidence the airfoil has bad performances. The rear airfoil is loaded most at design conditions. For positive or negative incidences i, a significant part of the load is shifted to the front airfoil, which makes it the most critical for off-design performance. Figure 7 shows the skin friction coefficient c_f distribution along the airfoils for the three different inlet flow angles:

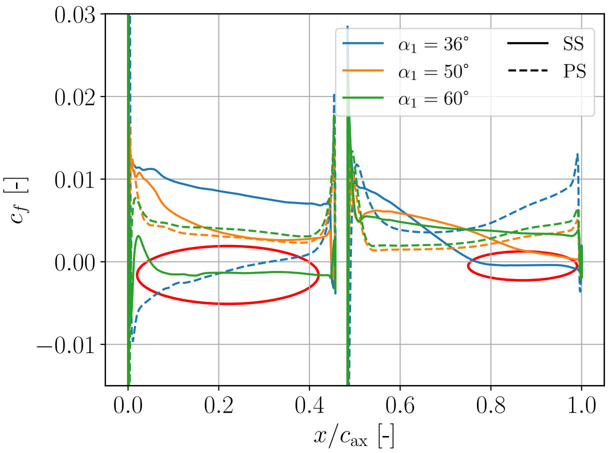

Figure 7: Skin-friction at $\chi_{rel} = 0$ and various α_1-angles.

$$c_f = \frac{\tau_w}{0.5\rho U_{in}^2}. \tag{2}$$

with τ_w the signed shear-stress along the airfoil and U_{in} the inlet velocity. The flow separation regions are highlighted by the red ellipse. At negative incidence (blue curve), the pressure side of the front airfoil undergoes into separation at 30% of the total chord. Consequently the rear airfoil suction side shows flow separation due to the congested gap between front and rear airfoil. At positive incidence (green curve) the front airfoil is almost fully separated, followed by an aft-located separation on the second airfoil. Both off-design conditions indicate the critical role of the front airfoil.

Figure 8, left-hand side axis, presents the evolution of pressure ratio $\pi = p/p_1$ along streamlines passing through the mid of the passage, whereas the mean flow path is shown in the top panel.

At nominal incidence (orange curve) the tandem airfoil can convert most of the kinetic energy into pressure. For negative incidence, (blue curve), the pressure drops dramatically and, despite it grows again towards the trailing edge, even does not reach the inlet pressure level when leaving the rear airfoil but goes into a second pressure drop.

Moreover, Figure 8, right-hand side axis, shows that the outlet flow angle does not reach zero after the airfoil passage at negative incidence. Despite the massive separation, the desired turning is obtained in the high-incidence case though, with a slight pressure decreases slightly towards the rear airfoil trailing edge.

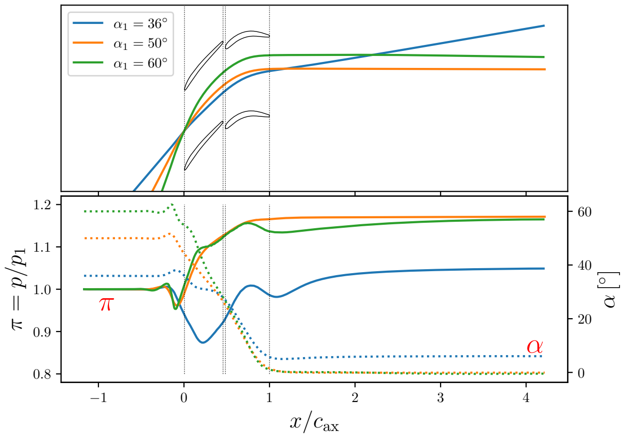

Figure 8: Streamline evolution of pressure ratio π (right y-axis, solid curves) and flow angle α (left y-axis, dotted curves).

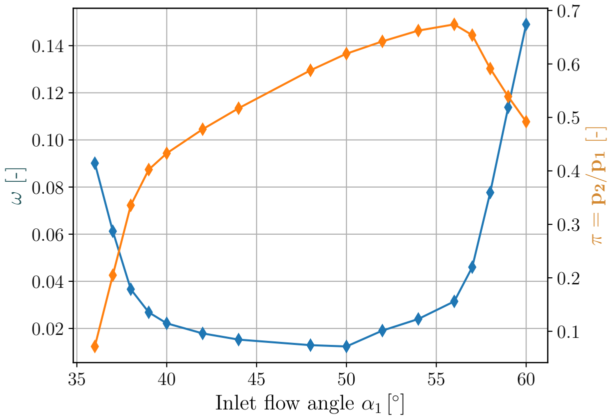

Figure 9: Loss coefficient ω (left y-axis) and pressure ratio $\pi = p_2/p_1$ (right y-axis)

Figure 9 shows the cascade polar, including the loss coefficient (blue curve) and pressure ratio (orange curve). The loss coefficient ω is defined as:

$$\omega = \frac{p_{0,1} - \widehat{p_{0,2}}}{p_{0,1} - p_1}, \tag{3}$$

where the $\widehat{*}$ symbols indicates a mass flow averaged quantity. The central region of the graph, around 47°, is characterised by low losses and high pressure ratio. Side regions are characterised by a decrease of performances featuring the typical dramatic increase of losses from given critical incidences onward. Figure 9 shows also the pressure ratio evolution (yellow curve). It can be noticed that in the classically designated stable range, corresponding to a loss level which is below twice the minimum, $(40° < \alpha < 55°)$, the pressure rise is approximately a linear function of incidence, whereas a dramatically rapid loss of performance is noticed outside of the stable operating range.

Figure 10 presents total pressure losses generated by the compressor stage. At design inlet flow angle, the wake consists of a peak in which the respective wakes of the two airfoils can be guessed from the small bumps. However, as we move

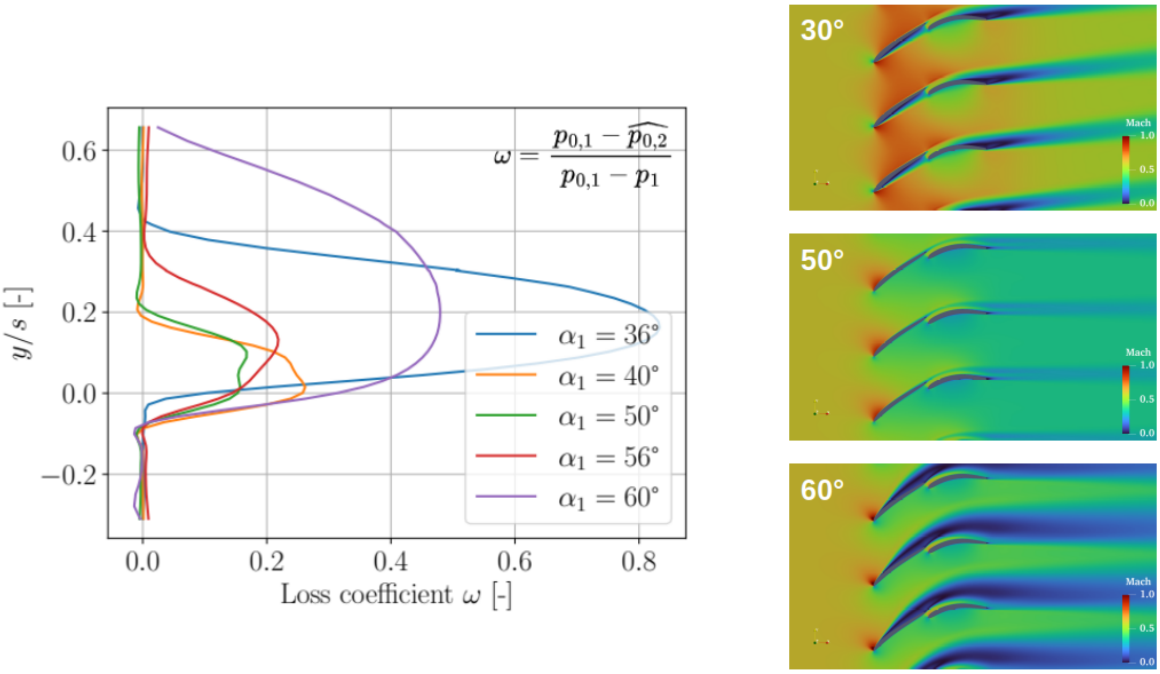

Figure 10: Loss coefficient ω along the pitch at outlet plane.

away from the reference incidence, the wake becomes wider and losses are higher. At negative incidence $\alpha_1 = 36°$, the wake remains relatively thin, but the losses within are approximately four times higher. This can be explained taking into account that the dissipation mechanisms are related (laminar) and modeled (turbulent) using velocity gradients. Negative incidence case is characterized by strong acceleration and deceleration, thus increasing the losses. Conversely, at positive incidence, the wake is much wider, although losses are lower than at negative incidence, spreading over most of the pitch and leaving little room for undisturbed flow to pass through.

Considering these results, and in particular the critical role of the front airfoil, the question arises whether would be possible to find a better tandem configuration using the same profiles, that allows to diminish the losses for high and low incidences, to increase the pressure ratio and hence to extend the operating range?

The present section suggests that there is some room for improvement, in particular in relation to the incidence on the front blade. We now investigate an approach in which we extend the idea of variable vane setting, usually used for intermediate stators (variable stator vanes) and apply it to the front blade alone, leading to the *variable front blade tandem (VFBT)*. In this way we maintain the outlet vane angle, and therefore retain the basic function of the OGV, while improving inlet incidence.

Unlike in the case the variable stator vanes, the choice of the pivot position is aerodynamically relevant since it determines the relative position of front and aft blade and potential conflicts. Therefore several variants are considered. For each of the pivot locations, the "optimal FB" loss-pressure rise polars are constructed, by retaining the best performance over the acceptable range of pivot angles (while keeping the Mach and Reynolds numbers constant).

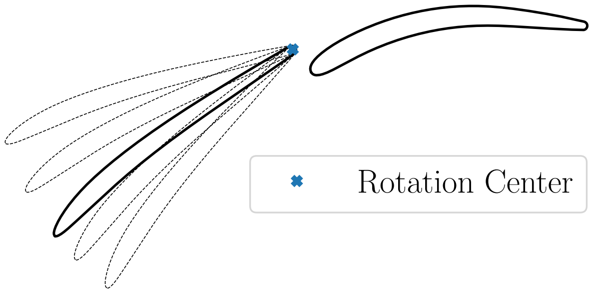

Figure 11: Front blade rotation around trailing edge.

5.2 Front Blade Rotation Around Its Trailing Edge

The first modification allows the front blade to rotate around its trailing edge curvature center as shown in Figure 11. This configuration is considered the most natural since the gap between the two blades is constant and there is no potential conflict between the blades. For every off-design incidence angle α_1, several front blade rotation angles $\chi_{\rm FB}$ will be investigated. The rotation angles, or stagger angles, will be referenced to the initial front blade configuration, which will therefore correspond to a zero degree front blade rotation angle, so that the relative rotation angle is given by

$$\chi_{\rm rel} = \chi'_{FB} - \chi_{FB} . \qquad (4)$$

The inlet flow angle range goes from 26 to 64 degrees. It is larger than the one used for the baseline study because the response of the tandem can be better to extreme inlet flow angles once an appropriate front blade rotation is applied. In other words, the rotation of the front blade extends the operating range of the tandem. A schematic of all the configuration simulated is shown in Figure 12. The figure is composed of 6 panels. Every panel includes two sub-figures displaced horizontally: at left-hand side is shown a schematic representation of the flow angle and the front blade actual position, when the front blade is rotated over the nominal angle, ie. the same angle as the flow with respect to the nominal setting ($\alpha_1 = 50°$). In the right-hand side graphs the losses are reported for as a function of front blade position χ_{Rel}, indicating the "nominal" rotation in red. At the top, in between the two panels the inlet angle α_1. By observing the figure, for many cases, the nominal front blade position, indicated by the red circle, is not the one characterised by lowest losses. Moreover, while the loss curve shape is rather smooth for moderate flow angles, its appearance is more irregular for extreme incidence angles. This fact suggests the possibility the flow might be rather complex challenging standard steady-state RANS models. However, more sophisticated techniques are not within the scope of this work, but will be considered in future work. Finally, Figure 13 shows the optimal angle of rotation of the front blade. It can be seen that, although the curve is not exactly linear, the optimum rotation follows the inlet flow angle, both in terms of losses and pressure ratio. There is also an interesting plateau in the negative incidence area, which is around $\chi_{\mathrm{rel}} = -12°$ for flow angles of 28 to 36 degrees.

The loss polar is represented in Figure 14 and the pressure ratio in Figure 15, compared to the original ones. These results only include the minimum loss and maximal pressure ratio obtained in Figure 12. The results obtained with the front blade rotation show a large extension of the operating range from $30° \leq \alpha_1 \leq 60°$, combined to a significant performance improvement even within the original incidence range, including the initial minimal loss coefficient. Secondly, the pressure ratio is now almost linear with respect to the inlet flow angle. An appropriate front blade rotation system around the trailing edge allows to gain 19° of incidence range with a lower minimal loss level. Finally, Figure 16 presents a contour plot of the Mach Number at high incidence for both the baseline configuration and the configuration after rotating the front blade to its optimal position.

5.3 Front Blade Rotation Around Camberline Midpoint

Although the airfoil performance related to the trailing edge actuation is impressive, this rotation point might present a serious drawback from a technological point of view. Indeed, the manufacturing of this kind of adjusting scheme would be rather difficult as the rotation axis should be attached to the blade in very narrow region of the blade. Moreover, the adjusting system would have to apply a important torque to maintain the blade in place. Therefore, different strategies are investigated to increase the OGV performances while keeping adjusting system feasible. This section focuses on the tandem front blade rotation around the midpoint of the camberline. This pivot promises a good compromise between aerodynamic performances and design feasibility. However, unlike the previous strategy, the gap (Δ_x, Figure 1) between front and rear blade does not remain constant, which introduces potential problems both in meshing and with the guidance of the flow in the overlap region.

A schematic representation of the airfoil rotation is shown in Figure 17. At rotation angles around -10 degrees, the tandem airfoils align and the overall airfoil row becomes similar to a single airfoil.

Figure 18 and 19 represent the loss ω and pressure coefficient π respectively. The orange curve represents the variable blade values, while the blue curves are the reference value of the baseline configuration. The incidence angle range is now $31° \leq \alpha_1 \leq 58°$. It appears that this adjusting strategy is very beneficial for both loss reduction and pressure ratio increase. Figure 20 shows the optimal rotation angles for each inlet flow angle, in terms of losses and pressure ratios. Although the general trend suggests an increase of the airfoils rotation with the flow angle for both loss and pressure ratio, it can be seen that this evolution is not fully linear. The pressure and loss curves qualitatively mimic each other, proving that in most cases, loss reduction and pressure gain are correlated. An interesting plateau is also observed around 45°: it seems that a airfoils rotation of $-2°$ is advantageous for both losses and pressure ratios. At low flow angles, once past the plateau at around $\chi_{\mathrm{rel}} = -2°$, the optimum angle drops directly to around $-12°$. In this configuration, the two blades are aligned and form a single blade (except for the small gap between them). It therefore appears that, at low inlet flow angles, the advantage of a variable tandem blade diminishes in favor of a fixed single blade.

5.4 Front Blade Rotation Around an Off-Blade Point

A third front blade actuation strategy is to select an external pivot point as shown in Figure 21. The aim is to keep a more constant gap between the airfoils. To determine the best point requires the solution of an optimization problem which will not be considered for the time being work; instead we consider the a rotation which results in a natural extension of the virtual camber line generated by both blades, which is approximated by choosing the opposite vertex in an equilateral triangle which has the front blade chord line as its base.

This center of rotation has the disadvantage of preventing almost all negative rotations because of the collision between the two blades. This strategy enables increases the incidence angle range up to 17.0°, and the optimal inlet flow angle is 48.1°.

The increase in incidence range is small with respect to the initial range (14.7°), although one should take into account that this increase in range is only obtained at positive incidence, since the blade could not be adapted to negative incidence for geometrical reasons; this was not deemed critical, as the positive incidence range is the most important for the stable operating range of the machine.

However, even when considering positive incidences only, the increase in performance and range is less than the other strategies under consideration. This conclusion may be im-

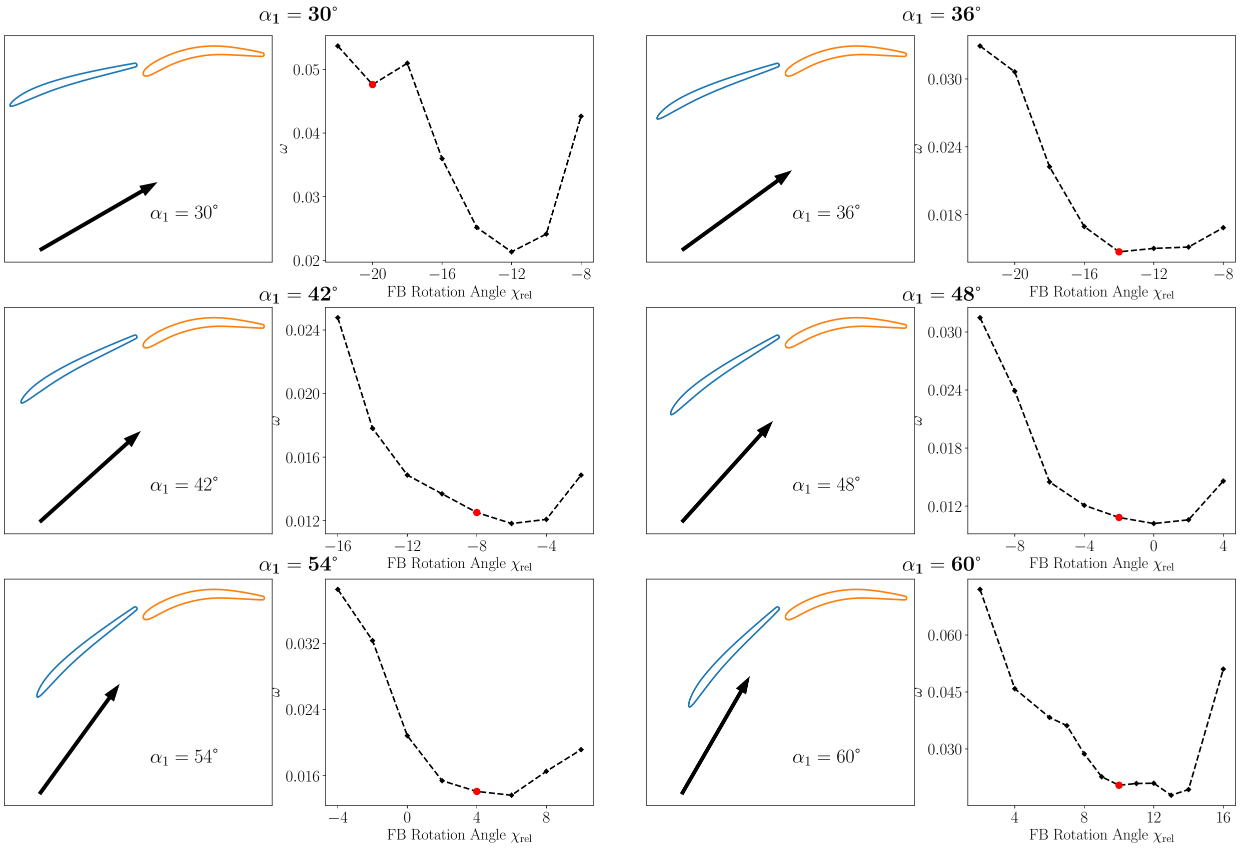

Figure 12: Rotation of the front blade around its trailing edge: losses for different inlet flow angles and blade position. Nominal rotation of the front blade, corresponding to the change of the inlet flow angle with respect to the nominal value, shown in the left graph, and indicated with the red dot in the loss graph.

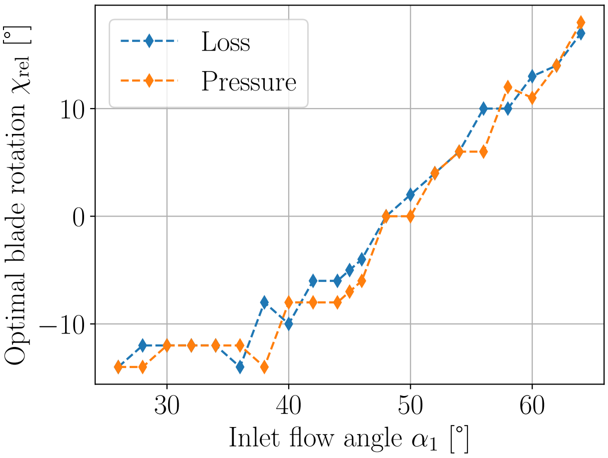

Figure 13: Optimal trailing edge rotation angle.

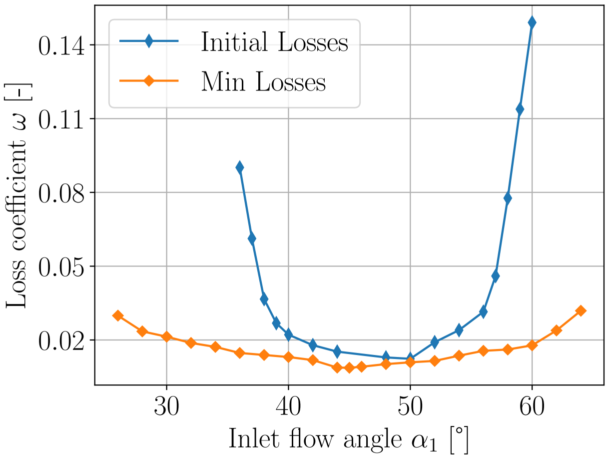

Figure 14: Rotation around trailing edge: loss coefficient comparison.

pacted by the peculiar shape of the front blade, which is almost uncambered, which seems unfavorable with respect to combined camber line; a combined optimisation of the front and aft blade camber line together with the pivot location will probably lead to further performance improvements with respect to the simple strategies studied in this paper.

In view of the disappointing results, this strategy will not be discussed independently, but will be compared to the other cases in the next section.

5.5 Comparison

The optimal losses are compared in Figure 22 with respect to the inlet flow angles, whereas the pressure rise is compared in figure Figure 23

Each of the strategies leads to significant increases in the

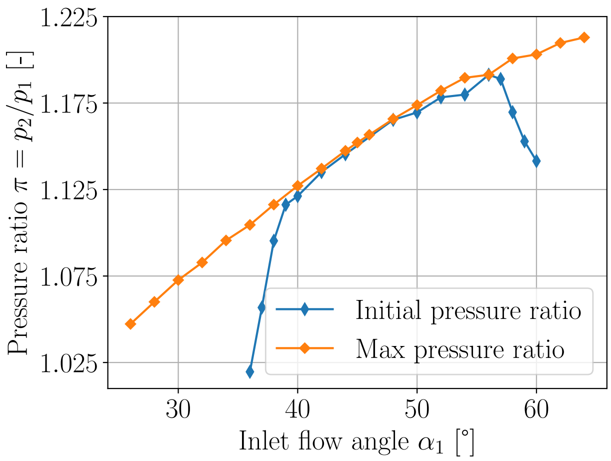

Figure 15: Rotation around trailing edge: pressure ratio comparison.

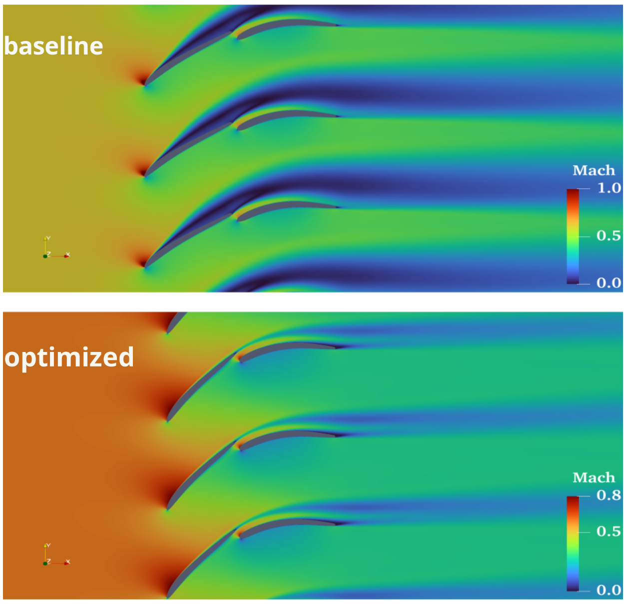

Figure 16: Rotation around trailing edge: Mach number for high incidence $\alpha_1 = 60°$, baseline and optimum front blade position.

incidence operating range.

At negative incidences, loss performances are comparable for trailing edge and midpoint rotation. The midpoint rotation provides slightly better results at very low flow angles, while trailing edge rotation is slightly better between 35° and 45°. However, in terms of pressure ratio, the trailing edge rotation performs the best.

From 45° onward, both losses and pressure ratios for all three strategies are similar up to 55°. However, at the higher flow angles, trailing edge rotation offers much lower losses while midpoint and external rotation behave similarly, with still slightly better performances for midpoint rotation. Moreover the pressure ratio at the highest flow angles is roughly the same regardless of the strategy used.

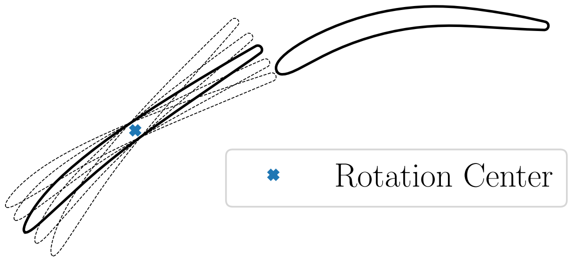

Figure 17: Front blade rotation around chord mid-point.

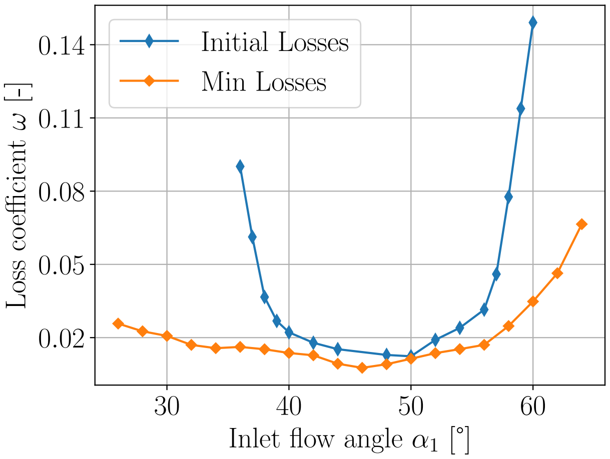

Figure 18: Rotation around chord mid-point: loss coefficient comparison.

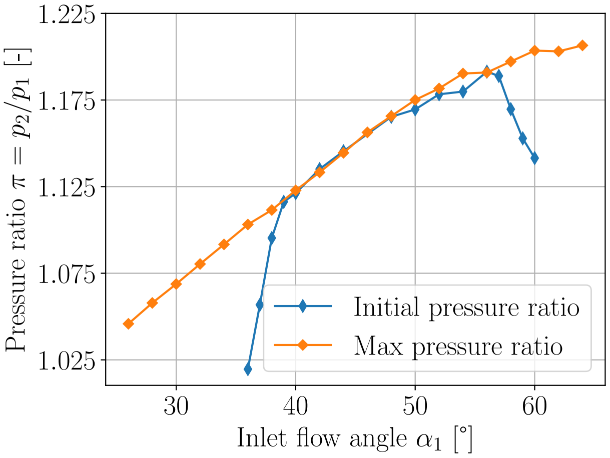

Figure 19: Rotation around chord mid-point: pressure ratio comparison.

6 Conclusion

The tandem blade, even in its fixed configuration, offers a promising design for outlet guide vanes (OGVs), enabling

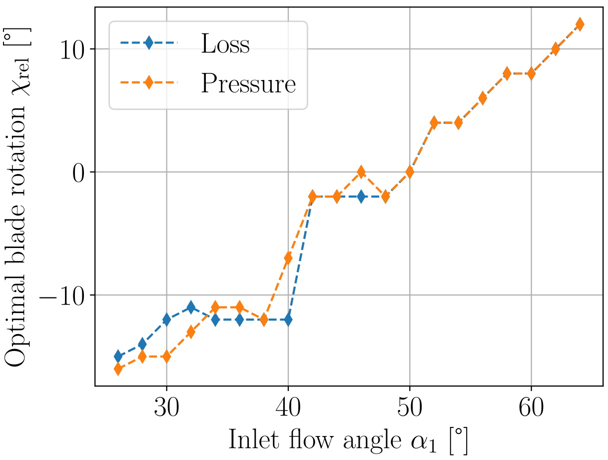

Figure 20: Rotation around chord mid-point: optimal rotation angle.

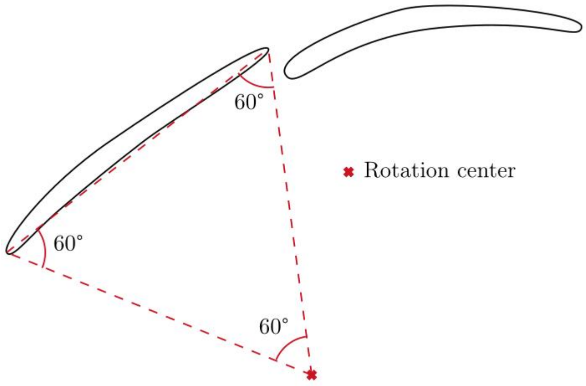

Figure 21: External rotation center schematic.

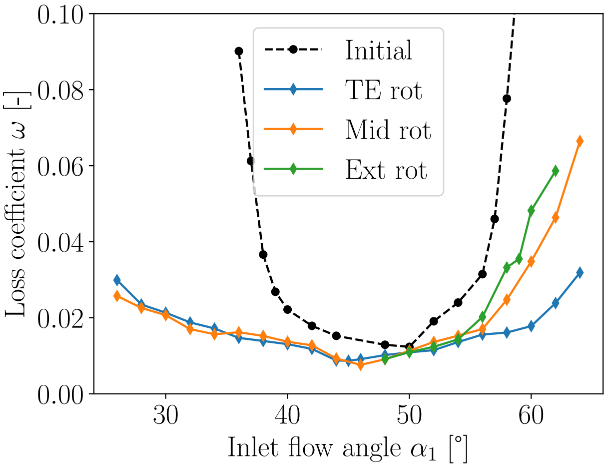

Figure 22: Overall losses comparison

high turning and recuperating axial outflow over a broader operating range compared to single blades. This potential is further enhanced by allowing independent adjustment of the leading-edge orientation through front blade pivoting, which maintains the outlet flow angle and extends the operating range.

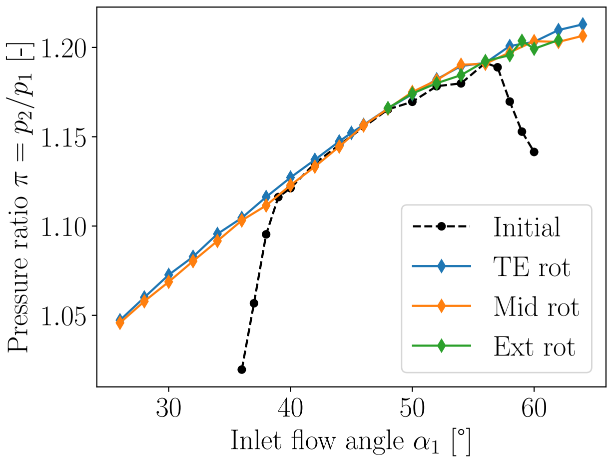

Figure 23: Overall pressure ratio comparison.

Fixed tandem configurations perform well at the design flow angle but show rapid performance deterioration—due to flow separation and suboptimal exit flow angles—as the incidence angle deviates. This restricts the incidence range to approximately 15°, beyond which losses double.

Numerical simulations explored extending the incidence range by altering the front blade's stagger angle via three strategies: rotation about the trailing edge, camberline midpoint, and the blade's approximate center of rotation. All strategies showed significant range improvements: 34.2°, 30.7°, and 17.4° respectively, with corresponding increases in pressure ratios for off-design incidences.

The trailing-edge rotation strategy yielded the best performance, particularly at high inlet flow angles, which are valuable for industrial applications due to higher pressure rises and proximity to surge conditions. However, this method poses significant implementation challenges, including high actuation torque and large pivot support requirements. The camberline midpoint strategy provides a practical compromise, balancing performance and feasibility.

In conclusion, variable tandem blades substantially expand the OGV operating range, especially at high flow angles. Ongoing optimization of the rotation point and blade shape aims to enhance both nominal and off-design performance.

Acknowledgments

This work is part of the WINGS (Walloon Innovations for Green Skies) project, launched in November 2020 and coordinated by Safran Aero Boosters. This is a three-year partnership project between 19 companies with the aim of tackling the ecological crisis affecting the aeronautical sector. An R&D budget is made available to contribute to the objectives of the European Green Deal and meet the low-carbon targets set out in the Paris Agreements. The three major companies in the Belgian aerospace sector (Safran Aero Boosters, Sonaca and Thales Belgium) are working on a series of varied research topics in collaboration with research centers (Cenaero, von Karman Institute, CRM, etc.) such as aerostructure, propulsion, communication systems, materials and processes, digitalization and digital simulation, and industry 4.0.

The present research benefited from computational resources made available on Lucia, the Tier-1 supercomputer of the Walloon Region, infrastructure funded by the Walloon Region under the grant agreement n°1910247. We also thank our colleagues at Cenaero for their contribution in the WINGS project and the anonymous reviewers for their comment.

Nomenclature

AO	axial overlap
c_{ax}	total axial chord
i	incidence angle
Ma	Mach number
p	static pressure
p_0	total pressure
PP	relative pitch
Re	Reynolds number
s	pitch
T_0	total temperature

Greek symbols

α_1	inlet flow angle
κ	blade metal angle
χ	blade stagger angle
ω	loss coefficient
π	pressure ratio

Acronyms

CFD	computational fluid dynamics
OGV	outlet guide vane
PS	pressure side
SS	suction side
VFBT	variable front blade tandem
VSV	variable stator vane

References

[1] L. Konrath, D. Peitsch, and A. Heinrich. "An Analysis of the Secondary Flow Around a Tandem Blade Under the Presence of a Tip Gap in a High-Speed Linear Compressor Cascade". In: *Journal of Turbomachinery* 144.10 (Apr. 2022), p. 101003. ISSN: 0889-504X. DOI: `10.1115/1.4051558`. eprint: `https://asmedigitalcollection.asme.org/turbomachinery/article-pdf/144/10/101003/6872372/turbo\_144\_10\_101003.pdf`.

[2] L. Konrath and D. Peitsch. "Impact of tip clearence variation of highly loaded tandem blades in axial compressors". In: *Proceedings of the ASME Turbo Expo*. June 2023.

[3] C. Tiedemann, A. Heinrich, and D. Peitsch. "Increasing Blade Turning by Active Flow Control and Tandem Configurations: A Comparison." In: *ISABE2017*. Sept. 2017.

[4] J. McGlumphy, W.-F. Ng, S. R. Wellborn, and S. Kempf. "Numerical Investigation of Tandem Airfoils for Subsonic Axial-Flow Compressor Blades". In: *Journal of Turbomachinery* 131.2 (2009).

[5] C. Hertel, C. Bode, D. Kozulovic, and T. Schneider. "Investigations on Aerodynamic Loading Limits of Subsonic Compressor Tandem Cascades: End Wall Flow". In: *Proceedings of the ASME Turbo Expo*. Vol. 2. June 2014. DOI: `10.1115/GT2014-26978`.

[6] T. Economon, F. Palacios, S. Copeland, T. Lukaczyk, and J. Alonso. "SU2: An Open-Source Suite for Multiphysics Simulation and Design". In: *AIAA Journal* 54.3 (2016), pp. 828–846.

[7] Geuzaine, Christophe and Remacle, Jean-Francois. *Gmsh*. Version 4.6.0. June 22, 2020.

[8] J. Ahrens, B. Geveci, and C. Law. "ParaView: An End-User Tool for Large Data Visualization". In: *Visualization Handbook*. ISBN 978-0123875822. Elesvier, 2005.

[9] U. Ayachit, A. Bauer, B. Geveci, P. O'Leary, K. Moreland, N. Fabian, and J. Mauldin. "ParaView Catalyst: Enabling In Situ Data Analysis and Visualization". In: *Proceedings of the First Workshop on In Situ Infrastructures for Enabling Extreme-Scale Analysis and Visualization (ISAV 2015)*. 2015, pp. 25–29. DOI: `10.1145/2828612.2828624`.

[10] U. Ayachit, A. C. Bauer, B. Boeckel, B. Geveci, K. Moreland, P. O'Leary, and T. Osika. "Catalyst Revised: Rethinking the ParaView in Situ Analysis and Visualization API". In: *High Performance Computing*. June 2021, pp. 484–494. DOI: `10.1007/978-3-030-90539-2_33`.

[11] F. M. White. *Fluid mechanics*. 6th ed. Mcgraw-Hill series in mechanical engineering. New York, NY: McGraw-Hill, 2009. ISBN: 978-0-07-352934-9.

[12] S. B. Pope. *Turbulent Flows*. Cambridge University Press, 2000.

[13] F. Menter, M. Kuntz, and R. Langtry. "Ten years of industrial experience with the SST turbulence model". In: *Heat and Mass Transfer* 4 (Jan. 2003).

[14] J. Eckel, A. Heinrich, C. Janke, J. Ortmanns, and D. Peitsch. "3D Numerical and Experimental Investigation of High Turning Compressor Tandem Cascade". In: *Deutscher Luft und Raumfahrtkongress 2016*. Sept. 2016.